Competing mechanisms of particle fracture, decohesion and slip-driven fatigue crack nucleation in a PM Nickel superalloy

Alexander Bergsmo[a], Fionn P.E. Dunne[a]

a) Imperial College London

Abstract

Fatigue cracks may initiate around non-metallic inclusions *via* particle fracture, particle decohesion and slip-driven nucleation. Cohesive zone techniques within microstructurally faithful crystal plasticity modelling validated by micromechanical experiments (HR-DIC and HR-EBSD) are employed to investigate these nucleation phenomena. Particle fracture and decohesion lead to stress redistribution which influences subsequent energy storage driving slip-driven fatigue crack nucleation. Particle fracture and decohesion strengths were determined and using a stored energy criterion, the number of cycles to initiation of the fatigue microcrack was predicted. A threshold applied stress below which decohesion and fracture do not occur was obtained, thus modestly increasing fatigue life.

Keywords: Crystal plasticity, non-metallic inclusions, fatigue initiation, Nickel Superalloy, Cohesive zone model

1 INTRODUCTION

Non-metallic inclusions can occur in polycrystalline Ni-base superalloy disc components produced via powder metallurgy, and are potentially important in influencing aero-engine component life times. Inclusions are incorporated in the powder from erosion of refractory oxides in contact with molten metal during the powder manufacturing process [1,2]. The powder is later hot isostatic pressed (HIPed), subjected to hot deformation to form billet, cut into forging multiples and isothermally forged to form near-net shape components with fine grained, homogenous grain structures [3]. Subject to cyclic loading regimes, commercial disc alloys with inclusions are known to nucleate cracks at a higher rate indicating that inclusions are detrimental to fatigue life [4]. While in this study we focus on fatigue crack nucleation within turbine disc alloys, fracture at non-metallic inclusions also remains a problem in other alloys; AM steels [5,6], SMA NiTi alloys [7], Steels [8] and Al alloys [9] are all known to contain inclusions and are relevant to fatigue.

Early studies of inclusions in disc alloys found them particularly detrimental to fatigue life in low cycle fatigue [1,10–12]. Jablonski [10] observed the effects of ceramic inclusions in low carbon Astroloy. The alloy was seeded with inclusions, HIPed and then subjected to a LCF regime. Fatigue cracks were found to originate at a higher rate from inclusions as temperature increased. In particular, oxide particles preferred to debond at 25℃ and crack at 500℃. Hyzak et al. [13] investigated low cycle crack nucleation in two nickel-base superalloys at room and elevated temperatures. A distinction between surface and internal nucleation from inclusions was made where high fatigue strain ranges correlated with surface nucleation and low strain ranges with internal nucleation. Crack nucleation originating from crystallographic facets dominated at room temperature. Therefore, crack nucleation at inclusions versus crystallographic facets are likely to be competing in nature. Chang et al. [11] investigated the origin and effect of different types of inclusions on LCF lifetimes. In addition, an effort was made to identify processing methods which negated the effects of inclusions. Thermomechanical processing was found to reduce and disperse the incidence of prior particle boundary (PPB) inclusions which were severely affecting the fatigue life. In the treated material however, unreactive ceramic inclusions continued to limit LCF lifetimes. Huron & Roth [2] deliberately seeded a Ni-base superalloy with inclusion populations of various sizes to investigate size sensitivity to nucleation rates. This study reinforced that fatigue cracking from inclusions at elevated temperature was significant. Probabilistic models for fatigue failure from inclusion defects have also been developed with good experimental agreement [14]. These models make the assumption that cracking from inclusions is

probabilistic in nature but do not elucidate the micro-mechanisms at play. Texier et al. [15] attempted to pre-fracture non-metallic inclusions with a monotonic load in order to characterise the role of pre-existing voids on crack nucleation behaviour. In samples with no pre-fracture, nucleation sites were predominantly in the vicinity of Σ3 twin boundaries due to the high elastic anisotropy in the crystal structure. In samples with fractured particles, nucleation occurred entirely from non-metallic inclusions.

Attempts were made to model nucleation events by Tanaka and Mura [16] who made enhancements to their existing dislocation dipole accumulation model to accommodate for initiation near hard particles. Distinctions were made between three modes of nucleation; decohesion of the metal-oxide interface, fracture of the particle, and slip bands emanating from an intact particle. Slip-driven nucleation was argued to occur when a critical value of self-strain energy was achieved due to dislocation dipole accumulation at the particle boundary. Inclusion fracture was addressed by use of the inclusion method of Eshelby [17]. Qualitative agreement was shown between published crack nucleation rates and model results but direct experimental validation at the micromechanical scale was not available.

Several studies have investigated the micromechanical drivers of fatigue crack nucleation in commercial Ni-base superalloys [18–22]. Zhang et al [20,21,23] investigated nucleation drivers in the disc superalloy RR1000 containing inclusions. Slip evolution during low cycle fatigue near an oxide agglomerate was captured by high resolution digital image correlation (HR-DIC) within a scanning electron microscope. Residual elastic strains and densities of geometrically necessary dislocations (GNDs) were captured using high angular resolution electron back scatter diffraction (HR-EBSD). Mismatching thermal expansivities between the inclusion and the metal matrix caused plastic hardening to occur adjacent to particles during the processing of the alloy. Densities of GNDs were noted to increase rapidly near particles as fatigue progressed and particle decohesion, fracture and slip-driven crack nucleation were observed, as shown in Figure 1 (a), (b) and (c) respectively. These nucleation modes are also illustrated schematically in Figure 1 (d).

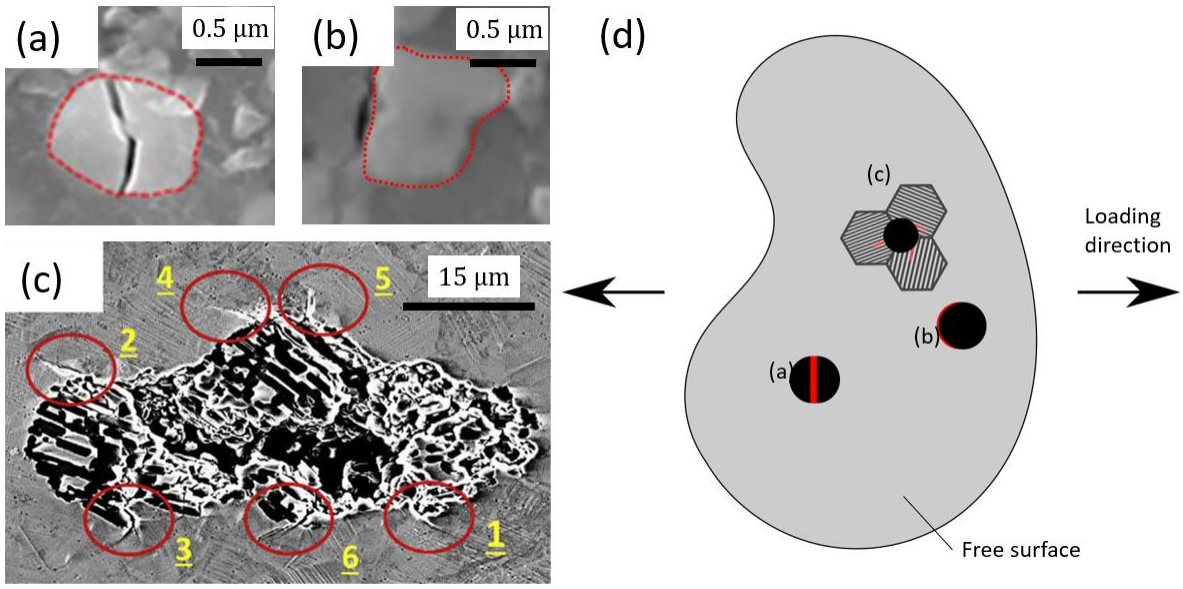

Figure 1, Micrographs of (a) particle fracture in Ni-base superalloy RR1000 [20], *(b) particle decohesion in RR1000* [20] *and (c) slip-driven crack nucleations from an inclusion in a Ni-base superalloy FGH96* [18]. *A schematic diagram of the nucleation modes is shown in (d)*

A subsequent study [21] used explicit representation of the local microstructures within a crystal plasticity finite element model of the inclusion region to investigate the effect of residual elastic strains, hydrostatic stress, effective plastic strain, stored energy density and normal stress on agglomerate-matrix decohesion. The study concluded that for the RR1000 alloy, for the loading conditions considered, the stress normal to the interface was unambiguously related to the metal-oxide decohesion. However, this work investigated only the quantitative drivers of agglomerate-matrix interface debonding and also did not expressly represent the decohesion process to account for stress redistribution. Fatigue crack nucleation in a similar but different alloy, FGH96, also containing inclusions [18,19] was found to occur by slip-driven processes in which residual stress and GND density at the location of crack nucleation were potentially found to be important [19]. Modelling studies of this alloy demonstrated that the sites of crack nucleation correlated directly with high magnitudes of stored energy density [18], where the latter is that fraction (arguably 5%) of plastic work which is stored in dislocation configurational energy (arising from dislocation structures) [24]. However, neither this nor the former study addressed the mechanistic drivers of the observed particle fractures, nor the potential coupling of particle-matrix decohesion, particle fracture, and slip-driven crack nucleation, and did not address the stress redistribution effects on slip-driven fatigue crack nucleation which occur through the physical processes of particle decohesion and particle fracture.

The cohesive zone model was conceived by Dugdale [25] and Barenblatt [26] to describe non-linear crack tip problems. In a contemporary cohesive zone model, surfaces (or elements) are assigned a traction-separation relation which describes the behaviour of fracture (or decohesion) as a load is applied. The approach is widely used to study delamination in composites [e.g. 27,28] but is applicable to any surfaces held together by cohesive forces. In the context of decohesion of second-phase particles, the method has been used to model elastic particles in an elastic-viscoplastic matrix [29], crystal plastic [30] matrix, silicon carbide fibre decohesion in metal matrix composites [28], decohesion of thermal barrier coatings [31], particulate decohesion in composites [27], and to investigate the influence of a surface oxide in microcantilever experiments [32]. Elzas et al. [33] implemented a cohesive zone model in a discrete dislocation plasticity framework and investigated crack growth at iron-precipitate interfaces.

The traction-separation behaviour is often characterised by maximum traction, displacement at failure and fracture energy (area under the traction-separation curve). The differing fracture behaviours from mode I to mode II are well known [34]. The cohesive zone model is therefore often described using mixed-mode relations [35]. The form of the traction-separation relationship is argued to be of utmost importance by several researchers [e.g. 42,49,50]. The physical significance of the relationship is in many cases based on atomistic predictions, including the exponential based curve of Needleman [29], related to fundamental work on binding energies of atomistically sharp planes by Rose et al. [38]. The exponential based curve is potential-based as it derives directly from the separation of atomic entities whereas non-potential shapes may be derived from phenomenological observations of fracture surfaces. The potential versus non-potential view is argued by Park et al. [39] who have recently introduced a generalised potential based cohesive zone model which is path dependent.

Three distinctive fatigue crack nucleation modes - particle decohesion, particle fracture and slip-driven nucleation – have been observed in relation to powder metallurgy nickel alloys containing agglomerates. Previous work has assessed the particle-matrix decohesion by quantitative study of interfacial normal stresses. However, the mechanistic basis of particle fracture (as opposed to decohesion) has not yet been quantitatively assessed. In addition, neither the particle-matrix decohesion nor particle fracture have been explicitly incorporated in to model microstructural representations in order to account for the stress redistribution which occurs from both mechanisms. Further, decohesion and particle fracture have not been investigated in terms of how they influence subsequent slip-driven fatigue crack nucleation and effect on fatigue life. Hence these are the objectives of this study which introduces cohesive zone modelling in to faithful polycrystal plasticity representations of an

experimentally characterised microstructure. Both particle-matrix decohesion and particle fracture are therefore allowed explicitly to occur such that the resulting stress redistributions and corresponding changes to stored energy density may be captured. The stress redistribution resulting from a particle fracture event, for example, then leads to significant changes to local interfacial normal stresses at an adjacent particle thereby radically changing the local driver for decohesion. Further, the stress redistributions resulting from both fracture and decohesion change the distributions and magnitudes of the stored energy density accumulations and hence the cycles required to give slip-driven fatigue crack nucleation. Hence the three failure mechanisms are shown to be strongly coupled. In addition, the mechanistic basis of experimentally observed particle fracture is addressed, revised interfacial particle-matrix cohesive strengths are obtained, and their influence on slip-driven crack nucleation investigated. This leads to the formulation of a preliminary mechanisms-based S-N curve for PM nickel alloys with agglomerated inclusions.

2 METHODS

2.1 CRYSTAL PLASTICITY FORMULATION

The crystal plasticity formulation used in this study is that reported in [40]. The deformation gradient, **F,** can be decomposed into contributions from the elastic $\mathbf{F}_e$ and plastic $\mathbf{F}_p$ components [41]. This relation can be written as:

$$\mathbf{F} = \mathbf{F}_e\mathbf{F}_p \tag{1}$$

The plastic component of the deformation rate is equal to the symmetric part of the plastic velocity gradient:

$$\mathbf{D_p} = \mathrm{sym}\left(\mathbf{L}_p\right) \tag{2}$$

The plastic velocity gradient, $\mathbf{L}_p$ may then be determined by:

$$\mathbf{L}_p = \dot{\mathbf{F}}_\mathrm{p}\mathbf{F}_\mathrm{p}^{-1} = \sum_{i=1}^{n} \dot{\gamma}^i(\mathbf{s}^i \otimes \mathbf{n}^i) \tag{3}$$

where i denotes the active slip system, **s** is the direction of dislocation slip, **n** is a normal to the slip plane and $\dot{\gamma}$ is the rate of crystal shearing (i.e. slip) given by:

$$\dot{\gamma} = \rho_{SSD}^{m} \nu b^2 \exp\left(-\frac{\Delta H}{kT}\right) \sinh\left(\frac{(\tau - \tau_{CRSS})\Delta V}{kT}\right) \quad 4$$

where ρ_{SSD}^{m} signifies the density of mobile statistically stored dislocations, ν is the frequency of jump events, b the burgers vector, ΔH the activation energy, k the Boltzmann constant, T the temperature, τ_{CRSS} the critical resolved shear stress, and ΔV is the activation volume. Isotropic hardening is incorporated by considering the development of statistically stored dislocations, $\dot{\rho}_{SSD}$, as the material is plastically strained.

$$\dot{\rho}_{SSD} = \lambda \dot{p} \quad 5$$

where λ is the hardening coefficient and $\dot{p}$ is the effective plastic strain rate. Slip system hardening may then be taken as Taylor hardening in iterative form:

$$\tau_c^i = \tau_{c_0}^i + Gb\sqrt{\rho_{SSD}} \quad 6$$

In this instance, $\tau_{c_0}^i$ refers to the initial intrinsic slip strength on the i^{th} slip system and G is the shear modulus of the material. A range of useful quantities can be determined from the crystal plasticity framework explained above. Effective plastic strain, p is given by:

$$p = \sqrt{\frac{2}{3}\mathbf{D}_{\mathrm{p}} : \mathbf{D}_{\mathrm{p}}} \quad 7$$

The stored energy density, which is that part of the plastic work which is stored by virtue of the establishment of dislocation structural interactions [24] over a length scale determined by the dislocation density, can be expressed as:

$$U = \int \frac{\xi \boldsymbol{\sigma} : d\boldsymbol{\epsilon}^p}{\sqrt{\rho_{SSD}}} \quad 8$$

where U is the stored energy density and ξ is the fraction of plastic energy in a cycle used to establish dislocation structures. This quantity has been used successfully to predict the location of cracks in polycrystal models and is discussed further in the next section.

2.2 Ni-base Superalloy Agglomerate model

In a previous study [20], a three-point bend specimen was subjected to low-cycle, load controlled fatigue. The specimen (12.7x3.5x1.94mm) was deliberately machined to contain an oxide agglomerate inclusion on the tensile fibre of the front, free face. In the experiment, developments of strains were recorded at interrupted intervals by using HR-DIC. In this study, a new explicit model representation of the agglomerate microstructure has been developed. This is related to that presented in [21] but very different in that it contains cohesive zone surface interactions to facilitate the study of agglomerate decohesion and fracture which have not been addressed before. The geometry was created from EBSD and SEM micrographs showing oxide particles, fine inter-oxide grains and coarse grains. As subsurface characterisation was not possible, edges were extruded to form columnar grains. This type of idealised model has been used in several prior studies with successful predictions of deformation [42,43]. Appropriate crystallographic orientations were applied to the coarser grains.

The small grains located between particles are numerous and obtaining accurate crystallographic orientations is difficult owing to their size. They are therefore assigned a reference orientation (i.e. the [1 0 0] pointing in x-direction and the [0 1 0] pointing in the y-direction). The oxide particles were identified as hafnia via SEM EDS. They were assigned elastic properties obtained from reported values in the literature [44]. Isotropic elasticity was assumed due to their size and difficulty in obtaining a surface finish sufficient enough to yield diffraction patterns. The properties are shown in Table 1. The ensemble was contained within an elastically isotropic medium representing the fine-grained, homogenous RR1000 microstructure. The physical properties used for the slip rule were obtained from calibration against tensile tests performed at Rolls-Royce plc. The resulting slip rule properties (equation 5) are shown in Table 2. Loading conditions local to the agglomerate region were inferred from a full beam model utilising von Mises plasticity, as described in [21] together with the independent experimental loading conditions and strain measurements.

Table 1, isotropic elasticity properties for Hafnia inclusions

E	G	ν
280 GPa	90 GPa	0.295

Table 2, the properties used for the slip rule.

ρ_{ssd}^{m}	b	ν	ΔH	T	τ_{crss}	λ	ΔV
0.05 μm^2	$3.51 * 10^{-4}$ µm	$1 * 10^{11}\ s^{-1}$	$3.456 * 10^{-20}$ J	293 K	450 MPa	150 μm^{-2}	$1.28b^3$

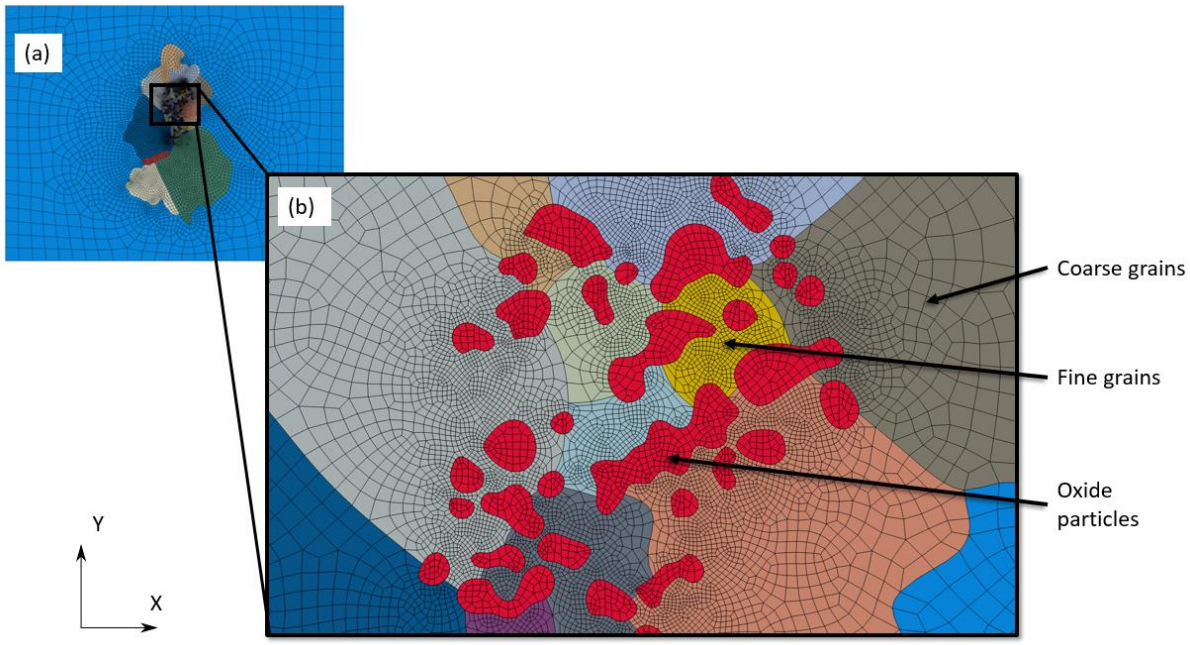

Figure 2, (a) Front-view mesh of the full crystal plastic submodel, (b) a detailed close-up of various microstructural features and their meshing within the submodel

The new microstructural model contains around 60,000 swept C3D20R finite elements representing the agglomerate oxide particles, and the coarse and fine Ni grains, and is shown in Figure , together with a close-up image to demonstrate the microstructural features captured. The mesh is refined local to the agglomerates since these are primary areas of interest in the present work. The crystal plasticity constitutive behaviour is incorporated through a user-material (UMAT) subroutine. Loading is applied on the right-hand surface to reproduce the load created in the 3pt-bend experiment as discussed in [21].

On surfaces separating oxide particles from Ni matrix, an interaction is defined using an elemental surface master-slave formulation with cohesive zone properties. This facilitates explicitly particle-matrix decohesion to be

modelled. In addition, surfaces are also created within oxide particles which have normals parallel to the direction of loading. These oxide-oxide interfaces are also assigned cohesive zone properties, and this enables particle fracture to be modelled independently. The cohesive zone model, and associated properties, used in this study are outlined in the next section. In total, 135 interactions are defined with an initial clearance between slave and master surfaces equal to zero. Example model predictions of local strain distributions along defined paths are shown in the appendix along with the independent experimental measurements taken from [21], showing reasonable agreement.

2.3 TRACTION-SEPARATION MODEL

Both particle fracture and decohesion are observed in the Ni-base superalloy agglomerate containing system. Here, we define traction-separation behaviour between selected oxide-oxide surfaces and metal-oxide surfaces to describe both particle fracture and decohesion respectively. *Decohesion* has been argued to occur only when the normal stress acting on the surface is sufficiently high [21]. It is therefore reasonable to assume that the tangential (mode II) and transverse (mode III) shear behaviours of the interface play little role in the decohesion and appropriately simplify the traction-separation behaviour by assigning relatively high tangential and transverse shear strengths, t_s^{max} and t_t^{max} respectively, while keeping the normal strength, σ_n^{max} physically representative of the true decohesion strength. The strength has been found to lie in the range of 1270 – 1480 MPa in terms of normal stress acting on the surface [21]; a parametric analysis is performed later in this study to investigate the validity of this range. Experimentally, it is observed that decohesion occurs in a brittle-manner where the stress carried normal to the interface eventually leads to the sudden decohesion of the metal-oxide interface. We postulate that the separation of surfaces is stress controlled. The shape of the traction-separation curve is therefore argued to be of secondary importance as, ideally, cohesion should cease after peak stress in reached. A bilinear traction-separation, originally developed by Geubelle et al. [45] and Alfano et al. [46] is therefore used. We define an initial traction-separation gradient, k_n, which is physically representative of the interfacial stiffness. Complete separation of surfaces is typically said to occur when traction reduces to zero subsequent to attaining its peak value. Here, we take decohesion to have occurred when the peak traction is attained. While there is little physical basis to assert that there is material continuity once this stress limit has been exceeded, rapid unloading of traction post-nucleation poses potential convergence problems for the three-dimensional finite element analysis. Convergence also becomes an issue when large slope changes are present. The elastic snap-back effect is mitigated here by adding a viscous regularisation term of μ =0.01 [47]. In addition, in the current geometric representation

of the microstructure, while decohesion may have occurred at the oxide-matrix interface on the sample free surface, the sub-surface material continues to provide constraint such that the average through-thickness normal stress remains finite and non-zero. These factors justify the need for a progressive linear interfacial unloading as shown in Figure (b). A separation distance, δ^f, is chosen such that the progressive linear unloading produces results reflective of experimental results.

Fracture of brittle particles is considered in a similar manner where a bilinear traction-separation is used with the assumption being that fracture is driven by a maximum principal stress. Surfaces are therefore orientated to be normal to the direction of loading (shown schematically in Figure (a)) with a σ_n^{max} term controlling the nucleation of fracture in a particle. The value of k_n is chosen to represent the elastic modulus of the oxide particle at the length scale of a micron. Properties for both *decohesion* and *fracture* are given in Figure (c).

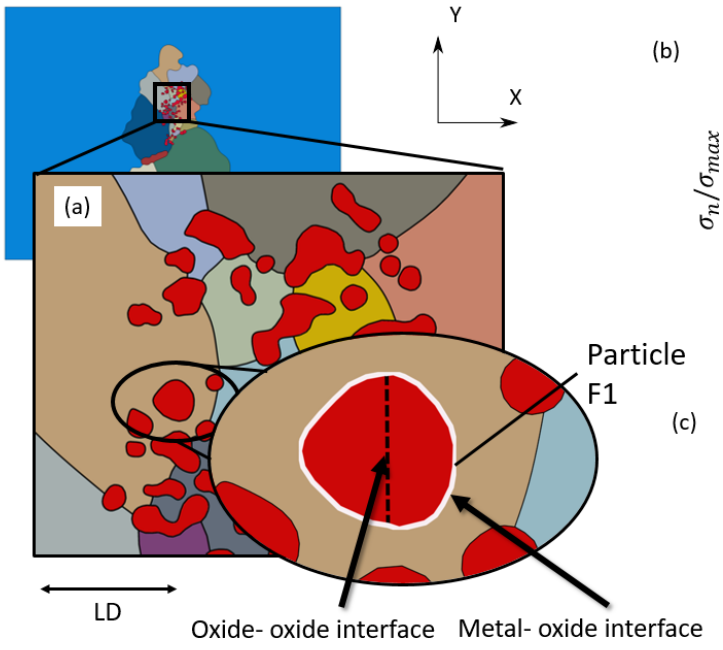

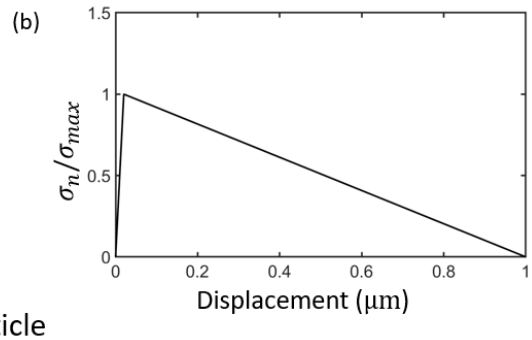

(c)

Property	Metal- oxide interface	Oxide-oxide interface
σ_{max} (MPa)	2050	2300
k_n (MNm^{-1})	210000	280000
δ^f (μm)	1	1

Figure 3, (a) Schematic example of the oxide-oxide (particle fracture) interface is displayed as the black, dashed line and metal-oxide (decohesion) interface which is shown in white for particle F1 (b) the traction-separation relation used, and (c) the properties used for particle fracture and decohesion

The traction-separation behaviour is implemented through the Abaqus surface interaction framework. The constitutive tensile behaviour of the cohesive zone is defined through contact separation and contact stress. In compression, no damage is accumulated and hard contact is defined.

3 FRACTURE STRENGTH OF OXIDE PARTICLES

The experimental observations reported in [21] showed that both particle fracture and particle decohesion occurred early during cyclic loading (within 1st -20th cycle). Figure shows those particles where fracture occurred and those for which decohesion occurred. In this section, the microstructurally representative crystal plasticity model established above is firstly used to investigate key quantities local to experimentally observed particle fractures in order to extract the mechanistic drivers for the particle fracture phenomenon rather than particle decohesion. This is carried out by studying the local behaviour prior to the occurrence of any particle-matrix decohesion or particle fracture. Explicit incorporation of the failure processes using cohesive zone modelling is addressed in a later section.

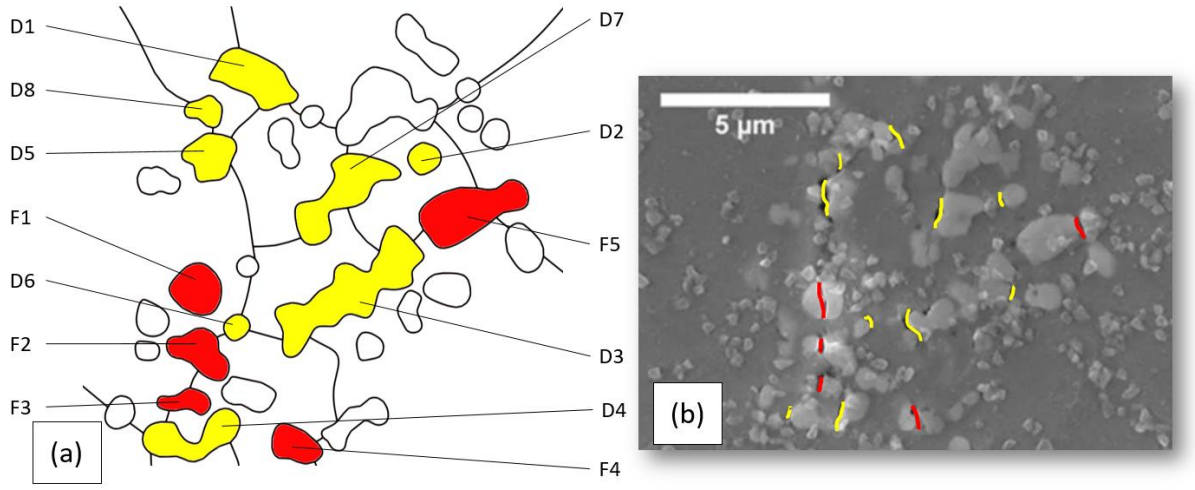

Figure 4, (a) trace of particles and grain boundaries in the agglomerate system with fractured particles highlighted in red and decohered particles highlighted in yellow. Annotations are provided for fractured particles (labelled F) and decohered particles (labelled D). (b) Experimental observation of the agglomerate region after loading with fracture and decohesion represented by red and yellow lines respectively, taken from [20]

Stresses normal to the particle-matrix interfaces around a range of particles have been extracted. Figure shows the predicted normal stress $\sigma_n = (\boldsymbol{\sigma}\mathbf{j}) \cdot \mathbf{j}$ (where **j** is a vector normal to the surface of a particle) distribution around particles which (a) and (b) decohered, and (c) and (d) fractured in the experimental observations shown in Figure . The stress is obtained here from the Ni integration points on the oxide boundary. The size of the arrow indicates magnitude of stress with red arrows indicating locations of maximum normal stress. Plots of stress magnitudes are given against the perimeter paths in Figure for (a), (b), (c) and (d) respectively. Cohesive interface strengths of 1270 – 1480 MPa previously reported in [21] are plotted on the graph. This range of decohesion strength was obtained by considering the mean normal stress of decohered particles at peak loading conditions

and comparing this value against peak normal stress of unaffected (non-decohered) particles. Stresses at peak loads are found to exceed the cohesive strengths indicating that decohesion should have occurred for all four particles (D1, D2, F1 and F2). For particles D1 and D2 (and others reported in [21]) the observed locations of decohesion are found to directly coincide with the location of peak normal stress in a significant number of decohered particles. The peak normal stresses were observed on interfaces which were normal to the direction of loading. Direct comparisons of predicted decohesion sites and experimental observations are shown in Figure with good agreement. However, particles which were observed to crack in the experiment (eg F1 and F2 discussed above and in Figures 5, 6) also develop high magnitudes of predicted interfacial peak normal stress, suggesting that they also should decohere unless, in fact, they had already fractured. This therefore suggests a quite separate mechanism is associated with particle fracture and that the local drivers were high enough to cause fracture before the interfacial stresses were high enough to drive decohesion. The variation of mean peak normal stresses during the peak load at the interface is investigated for particles which decohered in the experiment and particle which fractured in experiment. This is shown Figure .

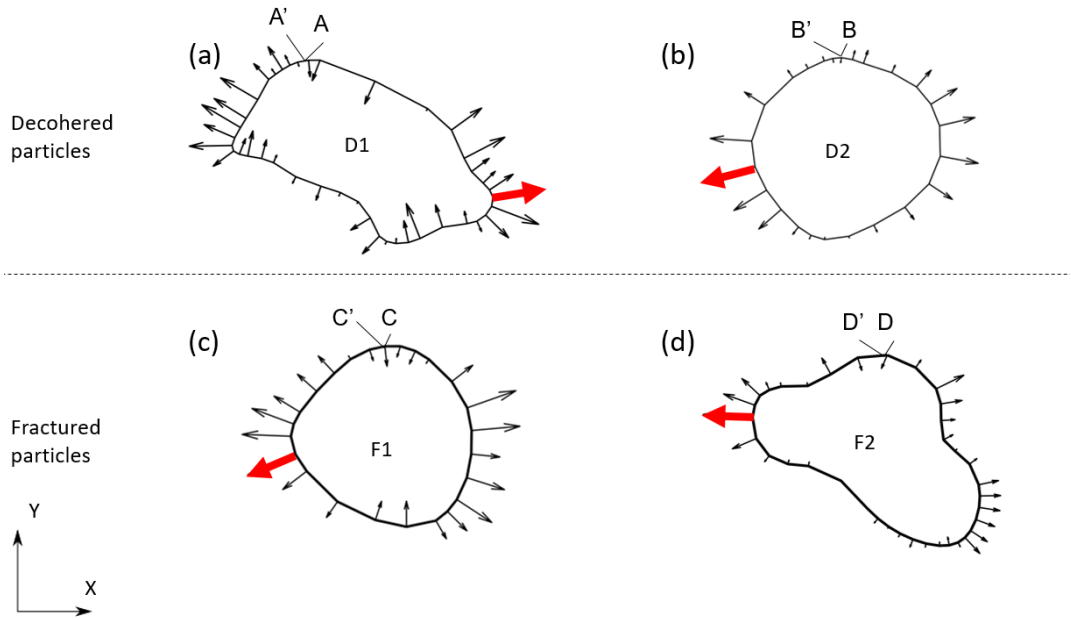

Figure 5, normal stress distributions with respect to the particle perimeters for which (a) and (b) are particles which decohere in experiment and particles (c) and (d) experience fracture after fatigue loading. Red arrows indicate the location of peak normal stress.

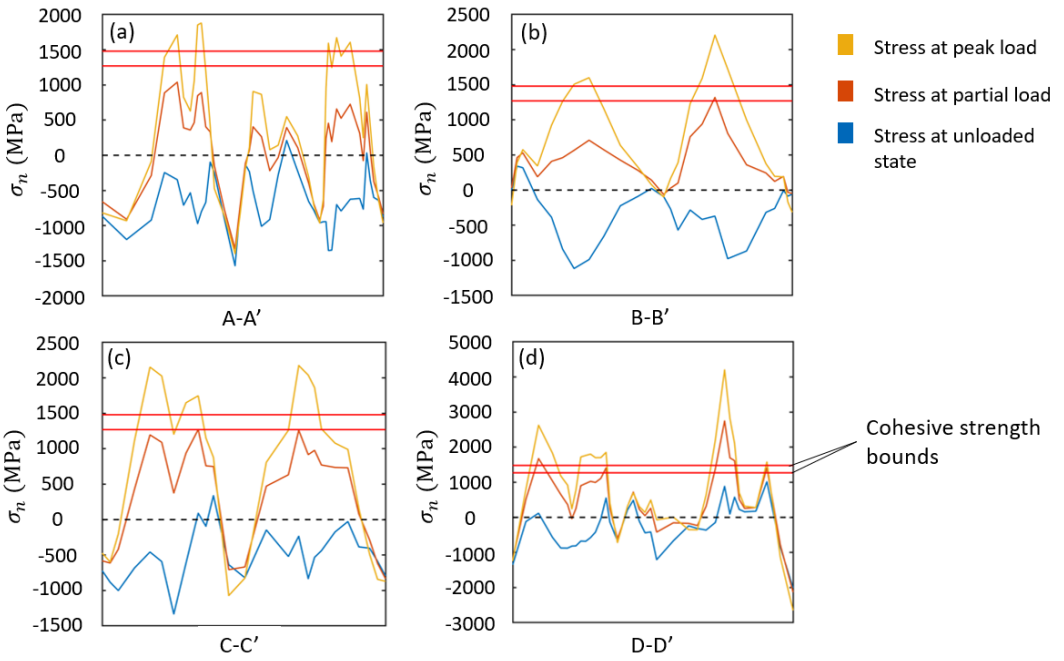

Figure 6, profiles of normal stress distributions during unloaded, peak and partial ($F = F^{max}\ 2/3$) loads of the first cycle around the perimeter of particles. Plots a), b), c) and d) correspond to respective plots in Figure . The previously reported cohesive strength range of 1270 -1480 MPa [21] *is plotted as red bands. (a) and (b) are for particles observed to decohere; (c) and (d) are for particles observed to fracture.*

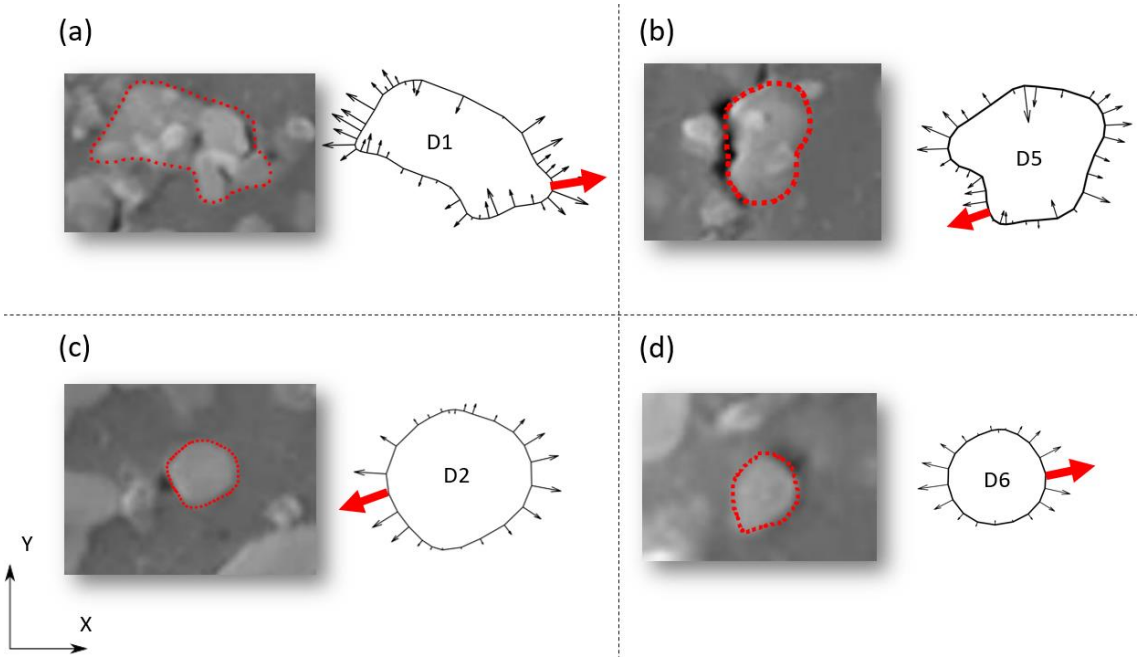

Figure 7, (a)-(d) Normal stresses on perimeter of particles are shown together with their corresponding experimental observations of particle matrix decohesion (from [21]*) after fatigue loading. Red arrows indicate point of maximum normal stress. (The smaller white particles partially visible are silica particles used as DIC speckles.)*

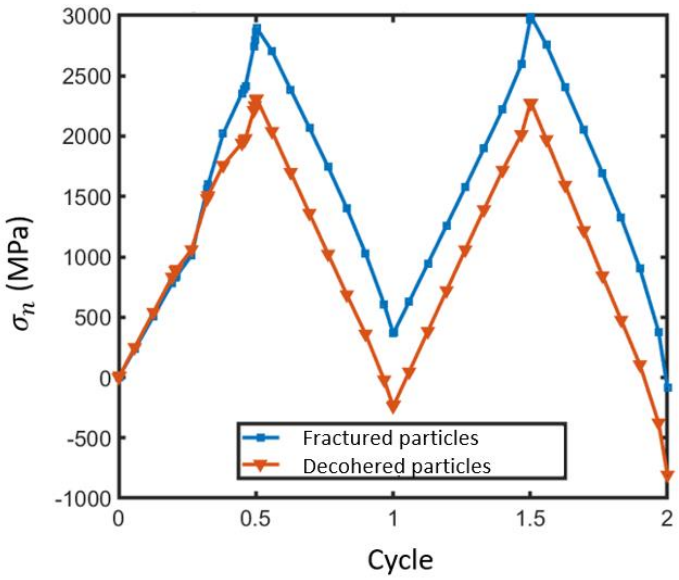

Figure 8, variation of particle mean of interfacial normal stress for particles which fractured in experiment and particles which decohered in experiment.

The perimeter normal stresses are predicted to be higher for fractured particles so we seek an alternative driver for particle fracture. Maximum principal stress was investigated as the potential primary driver of fracture in the brittle oxide particles. A maximum principal stress criterion of a Rankine type supposes that fracture occurs once a principal stress exceeds a critical value. Field plots of maximum principal stress are shown for the agglomerate region at the peak of the 1st cycle in Figure . Peak stresses are notably higher in the oxide particles due to their higher elastic modulus, and do seem to indicate the locations of particle fracture observed in experiments, as shown in Figure (b) and (c). Figure 2 shows arrow plots of the direction of maximum principal stress for the peak the first cycle. These are primarily orientated in the direction of loading during peak load. Some particles observed to fracture in experiments are predicted to be subject to large maximum principal stresses. Particles F1, F2, and F3 in particular are observed to have high maximum principal stresses in the direction normal to the fracture plane indicating strong agreement with experimental observations for these particles.

However, while the model predictions show some good agreement with experimental observations, it is not always the case as certain oxides which remain unfractured in the experiment are predicted to carry extremely high maximum principal stress. The model predictions indicate that some particles with high interfacial normal stress should fracture (as opposed to decohere) and some with high maximum principal stress should decohere (as opposed to fracture). However, it is well recognised that the process of particle-matrix decohesion and oxide fracture lead to stress redistribution and local relaxation which may significantly alter the local stress distribution in the region. For example, decohesion taking place at an interface orientated approximately normal to the primary

loading direction would have the effect of substantially reducing any axial (X-direction) stresses in the vicinity of the interface, thus reducing the propensity for both decohesion and particle fracture at adjacent particles lying along the same line of loading. Hence a more detailed and complete analysis is required to investigate and differentiate the mechanistic observations associated with particle decohesion and particle fracture, which explicitly accounts for the process and effect of the fracture and decohesion which occur. This is addressed in the next section.

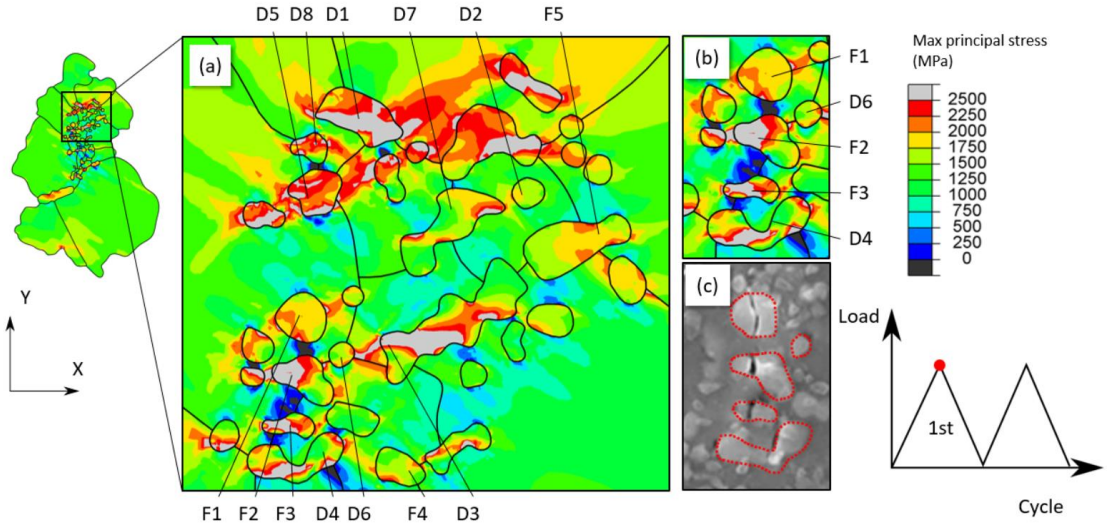

Figure 9, Field plot of maximum principal stress (a) at the peak of the first cycle, and (b) a corresponding close-up of the region with several fractured particles (F1, F2, F3), and (c) the corresponding SEM image shown after fatigue loading [20].

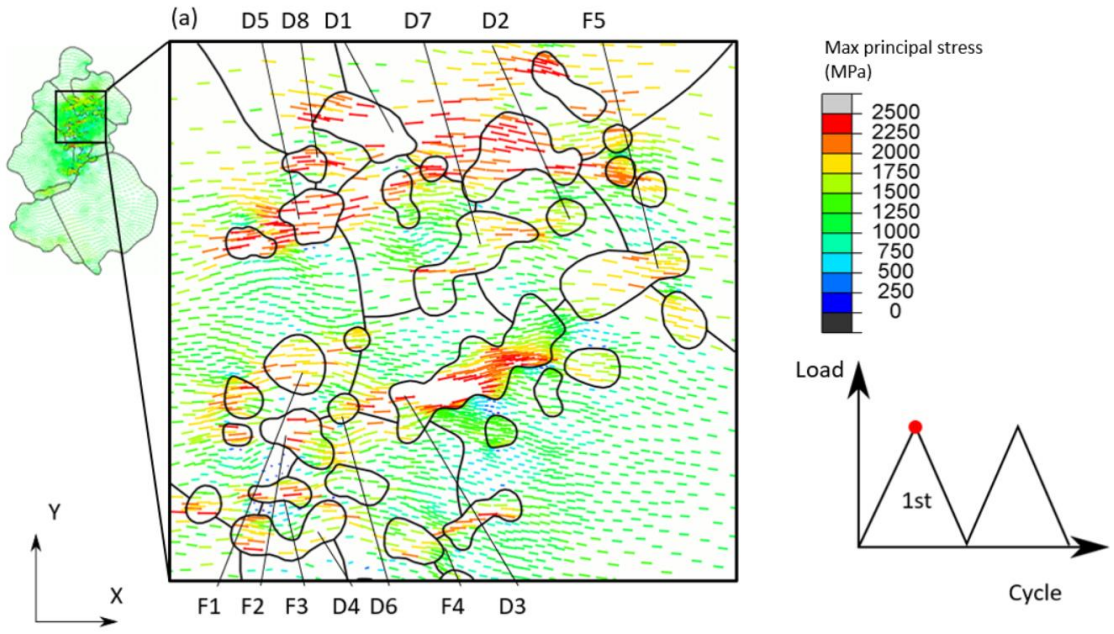

Figure 2, Maximum principal stress is plotted as arrows which indicate magnitude (size and colour) and direction for the peak of the first cycle.

4 MODELLING OF METAL-OXIDE INTERFACIAL DECOHESION AND PARTICLE FRACTURE USING COHESIVE INTERFACES

Cohesive zones are introduced at all metal-oxide interfaces and within oxide particles to investigate decohesion and particle fracture respectively in the agglomerate system. The microstructural agglomerate model utilised above and shown in Figure enhanced in this way was employed to carry out the study with the same loading conditions presented above. From the results obtained in Section 3 (for which explicit decohesion and particle fracture was not included), the oxide-matrix interfacial cohesive strength $\hat{S}_C$ was estimated to be 1270 MPa and the oxide particle fracture strength $\hat{S}_F$ to be 1580 MPa. However, the analysis incorporating explicit decohesion and particle fracture led to early failure of all interfaces (be they decohesion or fracture failures), demonstrating that the local interfacial normal stresses and intra-oxide maximum principal stresses exceeded the strengths given above. This indicates that both decohesion and fracture strengths are higher than previously estimated by the model which did not explicitly incorporate the failure processes. A sensitivity study (shown in Table 3) was therefore carried out using the microstructural model with a range of strengths for both $\hat{S}_C$ and $\hat{S}_F$. Careful

comparison of model results with the experimental observations of particle decohesion and intra-oxide fracture facilitated the extraction of more appropriate values for the strengths $\hat{S}_C$ and $\hat{S}_F$. The metal-oxide interfacial strength and oxide particle fracture strength were therefore determined in this way to be $\hat{S}_C$ = 2050 MPa and $\hat{S}_F$ = 2300 MPa respectively.

Table 3, the test matrix of the parametric study performed to find the interfacial strength $\hat{S}_C$, and the oxide strength $\hat{S}_F$

$\widehat{S}_C$ (MPa)	$\widehat{S}_F$(MPa)	**Qualitative results**
1270	1580	All interfaces damaged
1480	1800	All interfaces damaged
1800	1950	All interfaces damaged
2050	**2300**	***Partial interfaces damaged in keeping with experimental observations***
2050	2500	Damage pertaining only to metal-oxide interfaces

These strengths gave computed results in which the number of initiations of interfacial decohesion and particle fracture best reflected the experimental observations. Figure 3 (a) shows interfaces which are predicted to fail in the model. Note that the stresses acting on the interfaces peak within the first two cycles. The traction on metal-oxide and fracture interfaces then declines since some stress relaxation is observed in the vicinity of particles after the first few cycles. We therefore exclusively observe nucleation events within two cycles for the applied load considered. SEM micrographs of the corresponding topography after fatigue loading of 1000 cycles (Figure 3 (b)) show fractured particles [20], and in particular, as predicted by the model in Figure 3(a) in the particles labelled F1-F3. In this region, several particles fracture and are arranged in parallel with the direction of loading. The density and proximity of particles in this region are likely to drive locally high stresses which lead to the onset of particle fracture. Of the experimental particle fractures (F1 to F5) considered in the region of interest in Figure 3, four (F1, F2, F3, F5) were correctly predicted to fracture. Of the experimental oxide-matrix decohesions (D1 to

D8), three (D1, D3, D5) were predicted to decohere in this region. However, after the first cycle of loading at peak stress 1366MPa, the total number of experimentally observed particle failures events was 14, compared to a predicted total of 16. Of these, six were observed to be fractures and eight decohesions. The model predicted nine particle fractures and seven decohesions. Hence some of the experimental observations have been captured and it is clear that the hypothesised mechanisms (interfacial normal stress and particle maximum principal stress for decohesion and fracture failures respectively) do differentiate the observed failure types, even if not completely successfully in all cases. Regrettably, some of the experimental observations [21] are obscured by DIC speckles. A summary of the results is given in Figure 4

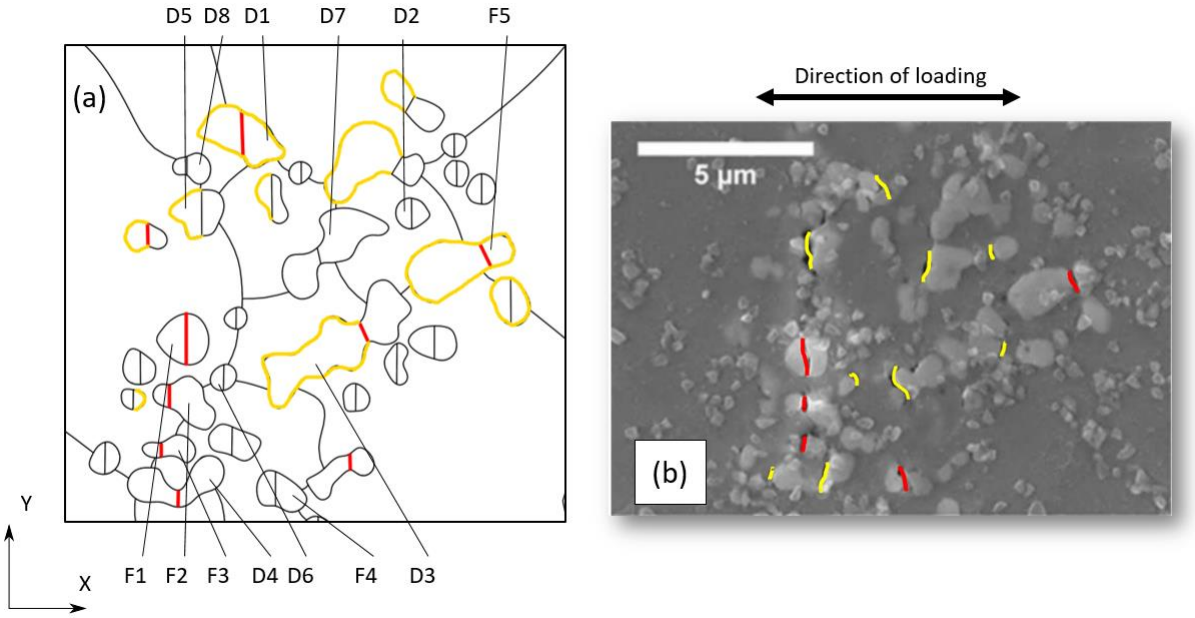

Figure 3, (a) Schematic of the interfaces predicted to fail (highlighted in red for fracture and yellow for decohesion). Failure is here defined as the peak normal traction exceeding the predefined strength of either fracture or decohesion. (b) Experimentally observed [21] *particle fracture (red) and decohesion (yellow) are annotated on a SEM micrograph of the corresponding region.*

(a)

Cycle	Parameter	Model	Experiment
	Failure events	16	14
	Cracks	9	6
1	Decohesions	7	8
	Failure events	21	14
	Cracks	10	6
2	Decohesions	11	8

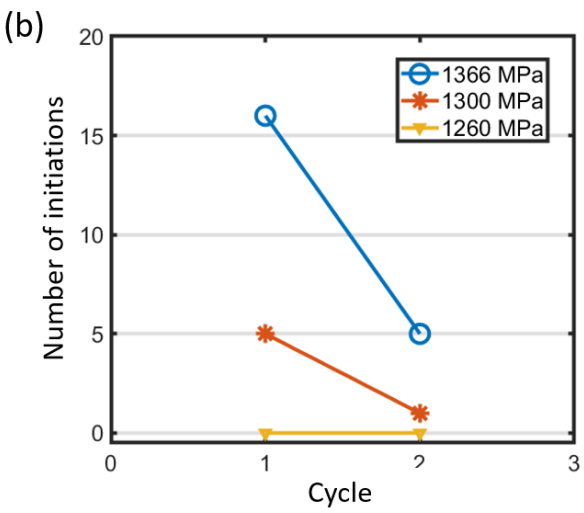

Figure 4, (a) the number of failure events (sum of fracture and decohesion) in the entire agglomerate region and their type predicted by the model and observed in experiment during the first and second cycles at a peak applied stress of 1366 MPa. (b) the model predicted number of failure events per cycle for differing applied loadings (1366, 1300 and 1260 MPa) demonstrating the dependence of failure on remote stress.

The model facilitates an investigation of the effect of applied stress magnitude on the nature (decohesion versus particle fractures) and number of failure initiations. In Figure 4, the model predicted number of failure events is shown for different applied peak loading for the first two cycles for applied peak stresses of 1366, 1300 and 1230 MPa respectively. The first cycle drives the largest number of failure events. A higher stress naturally causes a higher number of failure initiations to occur. Failure initiations were found to cease to occur (in both experiment and model prediction) after the second cycle. The frequency of initiation events is however extremely sensitive to the remote loading. A 5% drop in remote loading from 1366 MPa to 1300 MPa gives rise to an 80% drop in initiation events from 21 to 4 events. At 1230 MPa or 90% of original load, no initiation events are observed.

An abrupt change in decohesion and fracture events due to a decrease in applied stress suggests the failure mechanisms (fracture and decohesion) are sensitive to the strain-hardening properties of the material. A low strain-hardening would result in peak stresses occurring in early cycles. The material considered in this study shows relatively low strain-hardening and the failure mechanisms occur early. Early initiation is therefore likely stress-threshold based and a reduction of applied maximum stress would result in a change of failure mechanism. It is therefore possible to approximate a peak stress for which particle decohesion and fracture initiations do not occur at all and thus provide a solution to inhibit initiations of this type. In a high-strain hardening material, the expected response would be the development of significant plastic straining near the oxide/matrix interface. In such a

material, if early stresses are lower than the initiation threshold, then fracture and decohesion may occur subsequently in later cycles due to cyclic hardening.

Particle fracture and decohesion are processes which nucleate voids in the material and precede fatigue crack growth yet the onset of these phenomena is not sufficient to predict crack nucleation. Slip-driven crack nucleation occurs along persistent slip-bands impinging on the oxide/matrix interface. These cracks are different from particle fracture and decohesion in that they are crystallographic in nature and may therefore begin to grow immediately. In the experiment, it is observed that while fracture and decohesion occur early, a crystallographic fatigue crack does not nucleate until after 1000 cycles. Fracture and decohesion may therefore influence fatigue life, potentially redistributing stress and influencing the nucleation of slip-driven crack nucleation. The next section addresses the competition of nucleation between the particle fracture, decohesion and slip-driven initiations.

5 TOWARDS FATIGUE CRACK NUCLEATION MAPPING

Nucleation of fatigue cracks from non-metallic inclusions potentially originates from voids created by particle decohesion, particle fracture but certainly by slip-driven crystallographic fatigue crack nucleation. In this section we differentiate between the three nucleation modes mechanistically. We therefore utilise the criterion for crystallographic slip-driven nucleation introduced above in equation (8).

The stored energy density, U, has been shown to give quantitative predictions of fatigue crack nucleation sites and good prediction of fatigue life in steels [48] , Ni-base superalloys [49] and recently at non-metallic inclusions [18]. A critical stored energy density value, U_c, was introduced at which a fatigue crack is argued to nucleate. In [50], the critical stored energy density was determined for fine grained Ni alloy RR1000 to be 404 Jm^{-2}. The number of cycles to nucleation is found from

$$U_C = N_f \int \dot{U} dN \qquad 9$$

determined once the cyclic rate of stored energy accumulation has stabilised. In the present study, the stored energy density has been employed as the criterion for slip-driven fatigue crack nucleation. The agglomerate model above is utilised to investigate the role of the oxide particles, together with their decohesion and fracture, on stored

energy density evolution for the case of an applied load of 1366 MPa. After 10 cycles of loading in the model, the rate increase of stored energy density per cycle stabilises and it is therefore reasonable to extrapolate the stored energy rate at the end of this cycle and use equation 9 to find the fatigue life.

Figure 5 shows the predicted development of stored energy density in a model in which both decohesion and particle fracture are enabled (using the cohesive and particle fracture strengths from earlier). After the second cycle of loading, all decohesion and particle fracture events have taken place. Subsequent cycling then leads to the progressive evolution of stored energy density in the presence of the voids. Comparison is shown with the experimental microstructure where a crystallographic microcrack was found to nucleate between 1100 – 2000 cycles. The microcrack nucleation is localised in a region with predicted high stored energy density. Using $U_c = 404\ \mathrm{Jm}^{-2}$ as the criterion for microcrack nucleation, we find that the predicted cycles to fatigue crack nucleation are close to those obtained in the experiments [21]. A region that lies above particle D5 has a predicted nucleation lifetime of ~500 cycles and lies directly in the experimentally observed crack path. In the region above fractured particle F1, the model predicts a nucleation life of 1100 cycles.

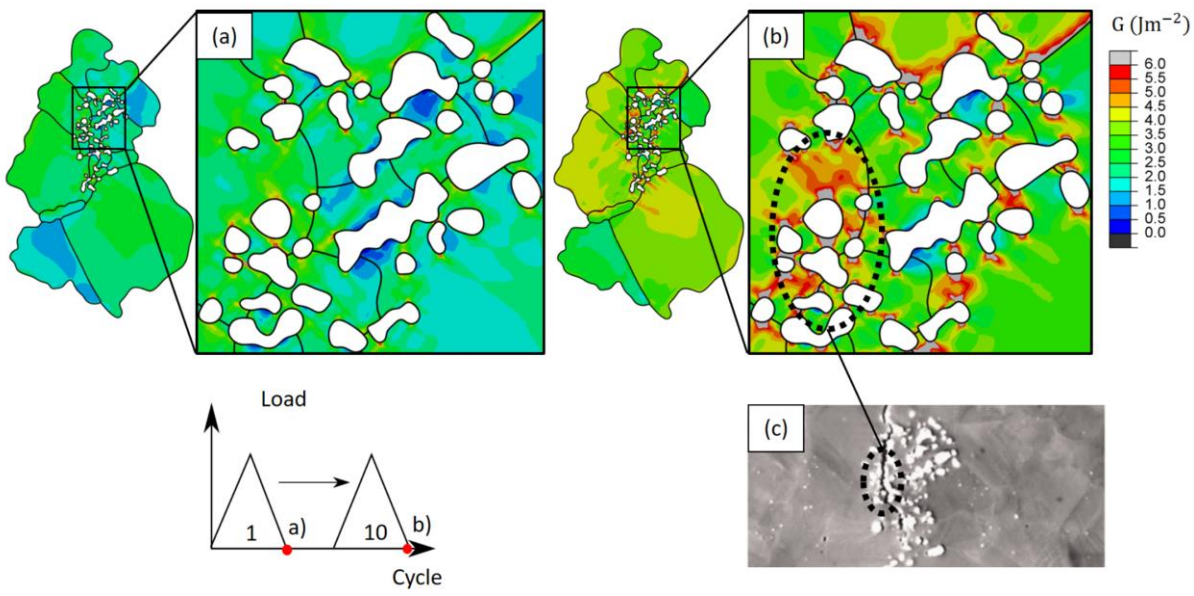

Figure 5, The development of stored energy density in a model utilising cohesive zones for capturing particle fracture and decohesion. (a) shows the stored energy density at the end of the first cycle and (b) after the 10th cycle. (c) shows the same region in an SEM micrograph after 2000 cycles of loading [21]

This shows some agreement with the experimental observations in which crack nucleation occurs between 1100-1900 cycles. Factors affecting crack nucleation behaviour which are not accounted for include gamma prime depletion near agglomerates, as well as sub-surface grain morphology and crystallography. The tertiary gamma

prime particles in the vicinity of particles are of the order of 40-50 nm. They likely influence the crack nucleation process but at a length scale smaller than that which has been investigated. Primarily, the gamma prime particles influence the slip resistance on a slip system and thus control the activation of slip and by extension slip banding. In a material system without large defect features such as inclusions, persistent slip bands and intrusions/extrusions will dominate the fatigue crack nucleation sites. In the present system, however, we argue that the influence of inclusions (which are sized on the order of 1-3 μm) on fatigue crack nucleation is much greater.

A field plot of predicted cycles to crack nucleation within the entire microstructure modelled based upon stored energy density is provided in Figure 6. Nucleation is predicted to occur exclusively near oxide particles. Locations above and below oxide particles, with the horizontal loading considered, are found to be most prone to crack nucleation. Particles F1, F2, F3, D1, and D5 lie on the nucleated microcrack site (see Figure 6) in the experiment which strongly suggests that their fracture (F) and decohesion (D) respectively drive the nucleation process.

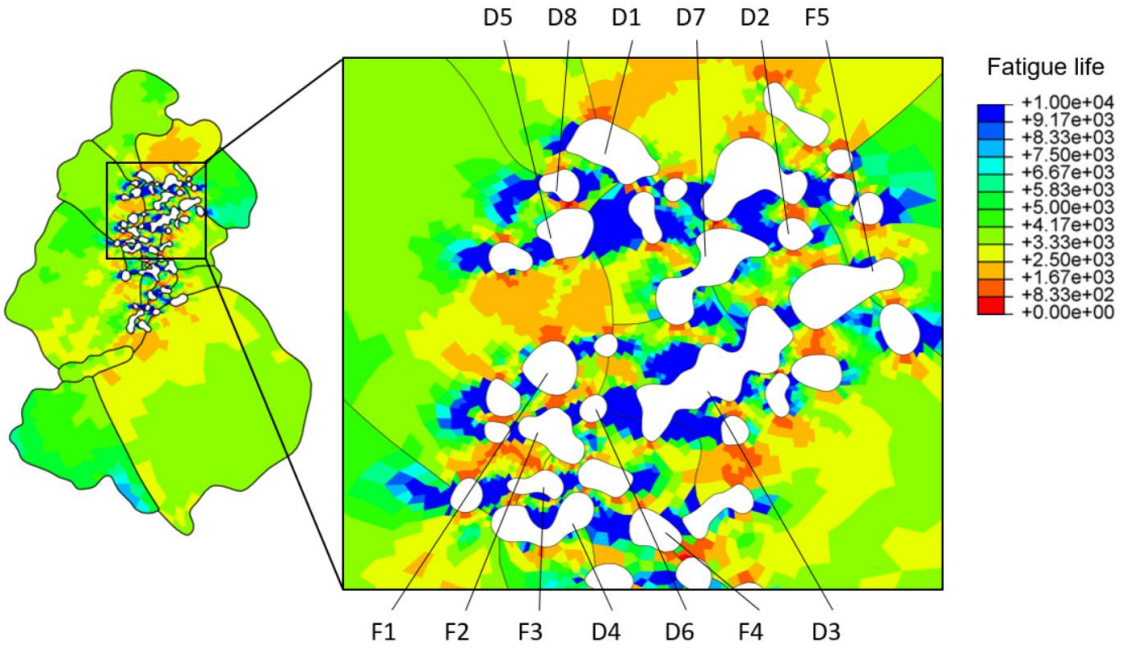

Figure 6, Predicted cycles to crack nucleation based on the stored energy density in a model incorporating particle decohesion and fracture. Experimental decohesion (D1-D8) and fracture (F1-F5) sites are labelled.

Slip-driven fatigue crack nucleation has been observed to occur in a different but related Ni alloy system containing inclusions [18]. Cracks develop at the metal-oxide interface and align with crystallographic planes with high slip accumulation. Local stress, slip accumulation and geometrically necessary dislocation density have all been shown to be important factors in this nucleation type but a high magnitude of local stored energy density has been found to unambiguously identify sites of crack nucleation. The agglomerate system considered in this paper exhibits decohesion and particle fracture early in the loading history, which have then linked by crystallographic slip-driven crack growth. The stored energy density has been shown to evolve significantly in the vicinity of the particles and is influenced by the decohesion and particle fracture. There is clearly an interplay between the three mechanisms. In order to investigate this further, we inhibit decohesion and particle fracture in the crystal plasticity model by assigning very high interfacial and fracture strengths such that the sole failure mechanism is slip driven fatigue crack nucleation and compare with the previous study.

A range of analyses with the same polycrystal agglomerate model were carried out with differing applied stress level (from 1500 down to 820 MPa) to obtain predicted cycles to slip-driven crack nucleation (taking $U_c = 404\ \mathrm{Jm}^{-2}$ as before) when both allowing particle fracture and decohesion and when inhibiting it. The results are summarised in Figure 7.

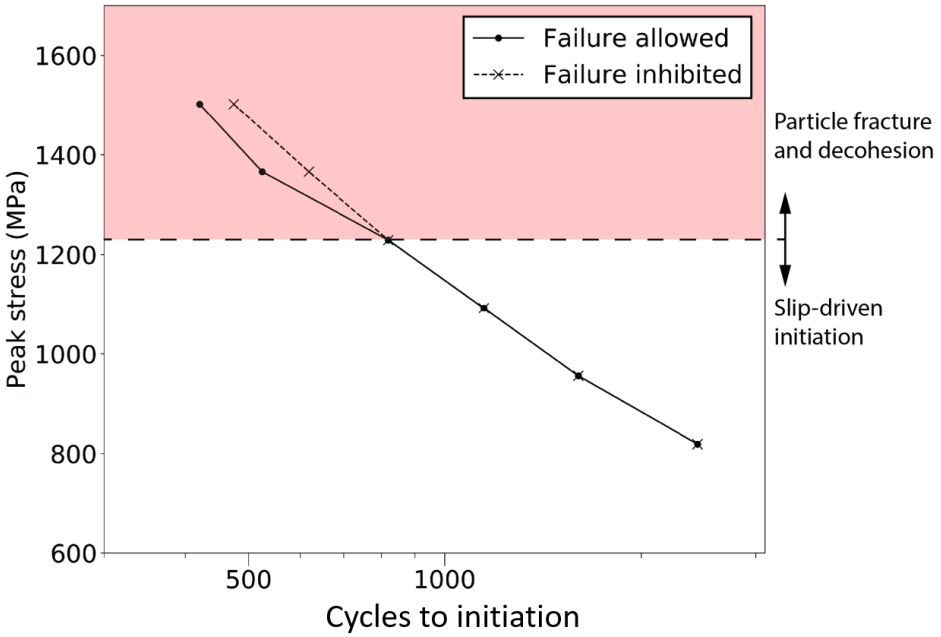

Figure 7, S-N plot for cycles to crack nucleation estimated from cyclic stored energy accumulation for the case in which failure (via particle fracture and decohesion) is allowed and for when it is inhibited. Particle fracture and decohesion do not occur below the stress threshold of 1230 MPa.

Particle fracture and decohesion have been shown to be stress dependent such that in a fatigue scenario with high stress, debonding and decohesion occur early, leading to a change in local stress and strain states and the corresponding stored energy density evolution with subsequent cycles. When neither debonding nor particle fracture occur, the rate of evolution of stored energy density at particles (but within the Ni matrix) is different, thereby changing the numbers of cycles to fatigue crack nucleation. In the case where decohesion and particle fracture occur, stored energy density is predicted to increase subsequently at a faster rate therefore leading to shorter fatigue lives. This is demonstrated in Figure 7 where predicted cycles to crack nucleation are plotted against applied cyclic peak stress for the cases in which debonding and fracture are allowed to occur and when they are inhibited.

While crack nucleation from inclusions dominate in this study, it is important to consider that crack nucleation may occur at other microstructural features within the same alloy. Several studies have shown that in alloys containing inclusions, nucleation may occur at grain boundaries rather than from particle decohesion and fracture, particularly at lower applied stresses [2]. At low applied stresses, Heinz et al. [51] have observed that fatigue crack nucleation originates from favourably oriented twin-boundaries with {1 1 1} slip systems activated parallel with the twin boundary. The origin of this phenomenon was argued to be due to the elastic incompatibility stresses and the ability for dislocations to travel relatively long distances along the twin boundary as opposed to neighbouring oblique grain boundaries. This observation has also been recorded by Stinville et al. [52] and Miao et al. [53] who have recorded twin boundary cracking in high-cycle fatigue. At lower stresses, it is therefore likely that the nucleation location shifts from non-metallic inclusions – for which decohesion and fracture are stress threshold dependent - to twin boundaries. A study is currently underway to investigate the competition between such microstructural features and their dependence on local hardening behaviour.

6 CONCLUSIONS

A microstructurally explicit oxide agglomerate-matrix model incorporating cohesive zone modelling of both particle/matrix interfacial decohesion and particle fracture has been developed for load-controlled fatigue in order to investigate the micromechanical drivers for crack nucleation observed in experiment on nickel alloy RR1000 containing oxide agglomerates.

High stresses normal to particle boundaries were found to be coincident with observed sites of oxide/metal decohesion reinforcing that interfacial normal stress is the controlling factor in decohesion. Analysis of stresses at peak loading conditions also revealed that particles observed to fracture in experiment are subject to the highest maximum principal stresses normal to the observed fracture planes. Both particle decohesion and fracture, modelled using cohesive zone formulations, were found to lead to the redistribution of stress within the microstructure, strongly influencing the stress states local to other oxide particles, in turn influencing the subsequent decohesion and fracture events. Explicit representation of the stress redistribution was found to be essential in order to capture the experimental observations. The oxide/metal interfacial strength and the oxide particle fracture strength were respectively found to be 2050 MPa and 2300 MPa. An upper bound applied stress therefore exists below which neither particle decohesion nor fracture occur.

Slip-driven fatigue crack nucleation was investigated using stored energy density. The latter was found to be influenced locally by particle/matrix decohesion and particle fracture which caused higher rates of stored energy accumulation and hence shorter fatigue life. Modelling studies showed that inhibiting particle/matrix decohesion and particle fracture increased fatigue life modestly. The critical energy density $404\ \mathrm{Jm}^{-2}$ determined in [45] was found to give predicted fatigue life times close to the present experimental observations, and to capture correctly the observed site of microcrack nucleation and growth.

Acknowledgements

The authors would like to acknowledge gratefully the financial support from EPSRC and Rolls-Royce plc. The authors are also grateful for helpful discussions with Mark Hardy, Paul Mignanelli and Christos Agyrakis.

Appendix A

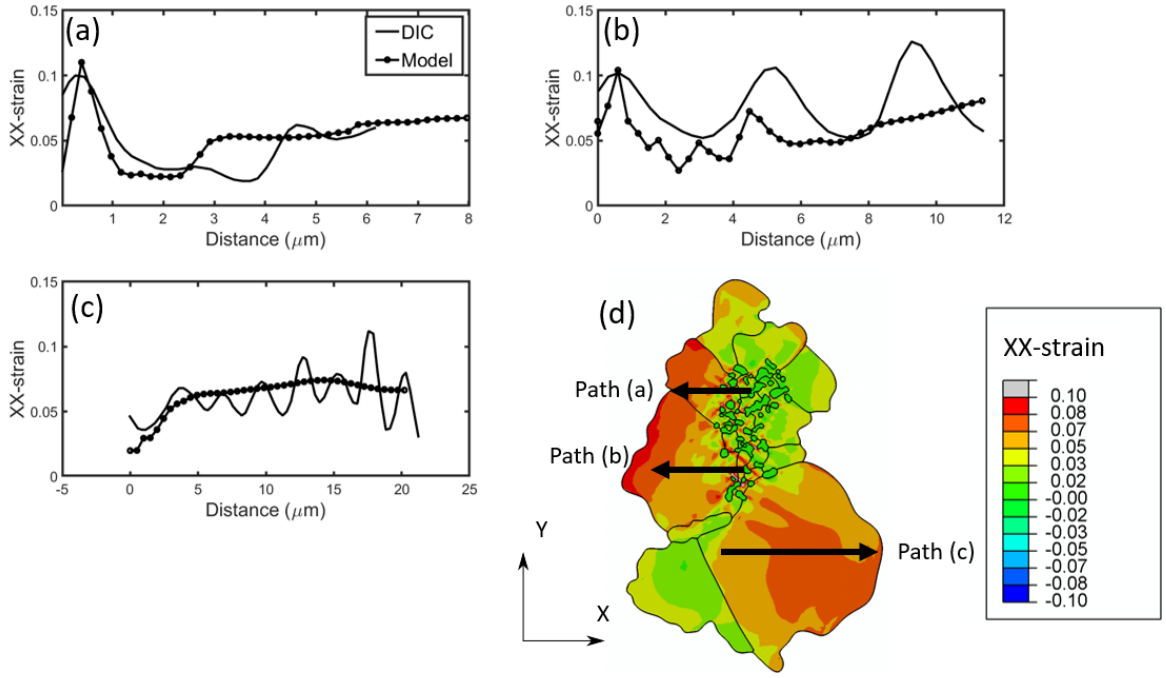

Figure A1, XX-strain across path profiles from DIC measurements [21], and model predictions. Figures a, b and c correspond to paths (a), (b) and (c) respectively

Figure *A1* shows variations of XX-strain after the second cycle of loading in the experiment obtained by DIC [21] and predicted by the CPFE model. Three paths are chosen showing relatively good agreement between experiment and model. Naturally, the HR-DIC technique (with sub-µm resolution) picks up highly localised slip activity which the crystal plasticity approach cannot but some of the key features and magnitudes of the strain distributions are captured.

References

[1] C.E. Shamblen, D.R. Chang, Effect of inclusions on LCF life of HIP plus heat treated powder metal rené 95, Metall. Trans. B. 16 (1985) 775–784. https://doi.org/10.1007/BF02667513.

[2] E.S. Huron, P.G. Roth, The Influence of Inclusions on Low Cycle Fatigue Life in a P/M Nickel-Base Disk Superalloy, Superalloys 1996. (1996) 359–368. https://doi.org/10.7449/1996/Superalloys_1996_359_368.

[3] R.C. Reed, The Superalloys Fundamentals and Applications, 2006. https://doi.org/https://doi.org/10.1017/CBO9780511541285.

[4] M.J. Caton, A.H. Rosenberger, J.M. Larsen, Divergence of Mechanisms and the Effect on the Fatigue

Life Variability of Rene' 88 DT, in: Superalloys, 2004: pp. 305–312.

[5] X. Lou, P.L. Andresen, R.B. Rebak, Oxide inclusions in laser additive manufactured stainless steel and their effects on impact toughness and stress corrosion cracking behavior, J. Nucl. Mater. 499 (2018) 182–190. https://doi.org/10.1016/j.jnucmat.2017.11.036.

[6] Y. Sun, R.J. Hebert, M. Aindow, Non-metallic inclusions in 17-4PH stainless steel parts produced by selective laser melting, Mater. Des. 140 (2018) 153–162. https://doi.org/10.1016/j.matdes.2017.11.063.

[7] A. Coda, A. Cadelli, M. Zanella, L. Fumagalli, Straightforward Downsizing of Inclusions in NiTi Alloys: A New Generation of SMA Wires with Outstanding Fatigue Life, Shape Mem. Superelasticity. 4 (2018) 41–47. https://doi.org/10.1007/s40830-018-0159-y.

[8] A. Weidner, T. Lippmann, H. Biermann, Crack initiation in the very high cycle fatigue regime of nitrided 42CrMo4 steel, J. Mater. Res. (2017) 1–12. https://doi.org/10.1557/jmr.2017.308.

[9] J. Fan, D.L. McDowell, M.F. Horstemeyer, K. Gall, Cyclic plasticity at pores and inclusions in cast Al-Si alloys, Eng. Fract. Mech. 70 (2003) 1281–1302. https://doi.org/10.1016/S0013-7944(02)00097-8.

[10] D.A. Jablonski, The effect of ceramic inclusions on the low cycle fatigue life of low carbon astroloy subjected to hot isostatic pressing, Mater. Sci. Eng. 48 (1981) 189–198. https://doi.org/10.1016/0025-5416(81)90004-5.

[11] D.R. Chang, D.D. Krueger, R. a. Sprague, Superalloy Powder Processing, Properties, and Turbine Disk Applications, Superalloys 1984 (Fifth Int. Symp. (1984) 245–273. https://doi.org/10.7449/1984/Superalloys_1984_245_273.

[12] T. Gabb, P. Bonacuse, L. Ghosn, J. Sweeney, A. Chatterjee, K. Green, Assessments of Low Cycle Fatigue Behavior of Powder Metallurgy Alloy U720, Fatigue Fract. Mech. 31st Vol. (2000) 110-110–18. https://doi.org/10.1520/STP14797S.

[13] J.M. Hyzak, I.M. Bernstein, The effect of defects on the fatigue crack initiation process in two p/m superalloys: part i. fatigue origins, Metall. Trans. A. 13 (1982) 33–43. https://doi.org/10.1007/BF02642413.

[14] J. Grison, L. Remy, Fatigue Failure Probability in a Powder Metallurgy Ni-base Superalloy, Eng. Fract. Mech. 57 (1997) 41–55. https://doi.org/10.1016/S0013-7944(97)00006-4.

[15] D. Texier, J. Cormier, P. Villechaise, J.C. Stinville, C.J. Torbet, S. Pierret, T.M. Pollock, Crack initiation sensitivity of wrought direct aged alloy 718 in the very high cycle fatigue regime: the role of non-metallic inclusions, Mater. Sci. Eng. A. 678 (2016) 122–136. https://doi.org/10.1016/j.msea.2016.09.098.

[16] K. Tanaka, T. Mura, A theory of fatigue crack initiation at inclusions, Metall. Trans. A. 13 (1982) 117–123. https://doi.org/10.1007/BF02642422.

[17] J.D. Eshelby, The determination of the elastic field of an ellipsoidal inclusion, and related problems, Collect. Work. J. D. Eshelby. (2007) 209–229. https://doi.org/10.1007/1-4020-4499-2_18.

[18] B. Chen, J. Jiang, F.P.E. Dunne, Is stored energy density the primary meso-scale mechanistic driver for fatigue crack nucleation?, Int. J. Plast. 101 (2018) 213–229. https://doi.org/10.1016/j.ijplas.2017.11.005.

[19] J. Jiang, J. Yang, T. Zhang, F.P.E. Dunne, T. Ben Britton, On the mechanistic basis of fatigue crack nucleation in Ni superalloy containing inclusions using high resolution electron backscatter diffraction, Acta Mater. 97 (2015) 367–379. https://doi.org/10.1016/j.actamat.2015.06.035.

[20] T. Zhang, J. Jiang, B.A. Shollock, T. Ben Britton, F.P.E. Dunne, Slip localization and fatigue crack nucleation near a non-metallic inclusion in polycrystalline nickel-based superalloy, Mater. Sci. Eng. A.

641 (2015) 328–339. https://doi.org/10.1016/j.msea.2015.06.070.

[21] T. Zhang, J. Jiang, B. Britton, B. Shollock, F. Dunne, Crack nucleation using combined crystal plasticity modelling , high-resolution digital image correlation and high-resolution electron backscatter diffraction in a superalloy containing non-metallic inclusions under fatigue Subject Areas :, Proc. R. Soc. A. 472 (2016) 20150792. https://doi.org/10.1098/rspa.2015.0792.

[22] D. Naragani, M.D. Sangid, P.A. Shade, J.C. Schuren, H. Sharma, J.S. Park, P. Kenesei, J. V. Bernier, T.J. Turner, I. Parr, Investigation of fatigue crack initiation from a non-metallic inclusion via high energy x-ray diffraction microscopy, Acta Mater. 137 (2017) 71–84. https://doi.org/10.1016/j.actamat.2017.07.027.

[23] T. Zhang, D.M. Collins, F.P.E.E. Dunne, B.A. Shollock, Crystal plasticity and high-resolution electron backscatter diffraction analysis of full-field polycrystal Ni superalloy strains and rotations under thermal loading, Acta Mater. 80 (2014) 25–38. https://doi.org/10.1016/j.actamat.2014.07.036.

[24] Z. Zheng, N.G. Prastiti, D.S. Balint, F.P.E. Dunne, The dislocation configurational energy density in discrete dislocation plasticity, J. Mech. Phys. Solids. 129 (2019) 39–60. https://doi.org/10.1016/j.jmps.2019.04.015.

[25] D.S. Dugdale, Yielding of steel sheets containing slits, J. Mech. Phys. Solids. 8 (1960) 100–104. https://doi.org/10.1016/0022-5096(60)90013-2.

[26] G.I. Barenblatt, The Mathematical Theory of Equilibrium of Crack in Brittle Fracture, Adv. Appl. Mech. 7 (1962) 55–129. https://doi.org/Last accessed: 14/04/2016.

[27] S.A. Ponnusami, S. Turteltaub, S. van der Zwaag, Cohesive-zone modelling of crack nucleation and propagation in particulate composites, Eng. Fract. Mech. 149 (2015) 170–190. https://doi.org/10.1016/j.engfracmech.2015.09.050.

[28] N. Chandra, H. Li, C. Shet, H. Ghonem, Some issues in the application of cohesive zone models for metal-ceramic interfaces, Int. J. Solids Struct. 39 (2002) 2827–2855. https://doi.org/10.1016/S0020-7683(02)00149-X.

[29] A. Needleman, A Continuum Model for Void Nucleation by Inclusion Debonding, J. Appl. Mech. 54 (1987) 525. https://doi.org/10.1115/1.3173064.

[30] X. Xu, A. Needleman, Void nucleation by inclusion debonding in a crystal matrix, Model. Simul. Mater. Sci. Eng. (1993).

[31] Y. Wei, J.W. Hutchinson, Toughness of Ni/Al2O3interfaces as dependent on micron-scale plasticity and atomistic-scale separation, Philos. Mag. 88 (2008) 3841–3859. https://doi.org/10.1080/14786430802311092.

[32] J. Dohr, D.E.J. Armstrong, E. Tarleton, T. Couvant, S. Lozano-Perez, The influence of surface oxides on the mechanical response of oxidized grain boundaries, Thin Solid Films. 632 (2017) 17–22. https://doi.org/10.1016/j.tsf.2017.03.060.

[33] A. Elzas, B. Thijsse, Cohesive law describing crack growth at iron/precipitate interfaces, Comput. Mater. Sci. (2017). https://doi.org/10.1016/j.commatsci.2017.01.042.

[34] T.L. Anderson, FRACTURE MECHANICS Fundamentals and Applications, Angew. Chemie Int. Ed. (2001). https://doi.org/10.1002/1521-3773(20010316)40:6<9823::AID-ANIE9823>3.3.CO;2-C.

[35] M.L. Benzeggagh, M. Kenane, Measurement of mixed-mode delamination fracture toughness of unidirectional glass/epoxy composites with mixed-mode bending apparatus, Compos. Sci. Technol. 56 (1995) 439–449. https://doi.org/https://doi.org/10.1016/0266-3538(96)00005-X.

[36] A. Needleman, An analysis of tensile decohesion along an interface, J. Mech. Phys. Solids. 38 (1990) 289–324. https://doi.org/10.1016/0022-5096(90)90001-K.

[37] V. Tvergaard, J.W. Hutchinson, The relation between crack growth resistance and fracture process parameters in elastic-plastic solids, J. Mech. Phys. Solids. 40 (1992) 1377–1397. https://doi.org/10.1016/0022-5096(92)90020-3.

[38] J.H. Rose, J. Ferrante, J.R. Smith, Universal binding energy curves for metals and bimetallic interfaces, Phys. Rev. Lett. 47 (1981) 675–678. https://doi.org/10.1103/PhysRevLett.47.675.

[39] K. Park, G.H. Paulino, J.R. Roesler, A unified potential-based cohesive model of mixed-mode fracture, J. Mech. Phys. Solids. 57 (2009) 891–908. https://doi.org/10.1016/j.jmps.2008.10.003.

[40] F.P.E. Dunne, D. Rugg, A. Walker, Lengthscale-dependent, elastically anisotropic, physically-based hcp crystal plasticity: Application to cold-dwell fatigue in Ti alloys, Int. J. Plast. 23 (2007) 1061–1083. https://doi.org/10.1016/j.ijplas.2006.10.013.

[41] E.H. Lee, Elastic-Plastic Deformation at Finite Strains, J. Appl. Mech. 36 (1969) 1. https://doi.org/10.1115/1.3564580.

[42] A.D. Rollett, A.M. Maniatty, J.E. Bozek, A.R. Ingraffea, D.J. Littlewood, M.G. Veilleux, J.D. Hochhalter, A geometric approach to modeling microstructurally small fatigue crack formation: III. Development of a semi-empirical model for nucleation, Model. Simul. Mater. Sci. Eng. 19 (2011) 035008. https://doi.org/10.1088/0965-0393/19/3/035008.

[43] L. Wang, R.I. Barabash, Y. Yang, T.R. Bieler, M.A. Crimp, P. Eisenlohr, W. Liu, G.E. Ice, Experimental characterization and crystal plasticity modeling of heterogeneous deformation in polycrystalline α-Ti, Metall. Mater. Trans. A Phys. Metall. Mater. Sci. 42 (2011) 626–635. https://doi.org/10.1007/s11661-010-0249-8.

[44] J. Wang, H.P. Li, R. Stevens, Hafnia and hafnia-toughened ceramics, J. Mater. Sci. 27 (1992) 5397–5430. https://doi.org/10.1007/BF00541601.

[45] P.H. Geubelle, J.S. Baylor, Impact-induced delamination of composites: A 2D simulation, Compos. Part B Eng. 29 (1998) 589–602. https://doi.org/10.1016/S1359-8368(98)00013-4.

[46] G. Alfano, M.A. Crisfield, Finite element interface models for the delamination analysis of laminated composites: Mechanical and computational issues, Int. J. Numer. Methods Eng. 50 (2001) 1701–1736. https://doi.org/10.1002/nme.93.

[47] Y.F. Gao, A.F. Bower, A simple technique for avoiding convergence problems in finite element simulations of crack nucleation and growth on cohesive interfaces, Model. Simul. Mater. Sci. Eng. 12 (2004) 453–463. https://doi.org/10.1088/0965-0393/12/3/007.

[48] V.V.C. Wan, D.W. Maclachlan, F.P.E. Dunne, A stored energy criterion for fatigue crack nucleation in polycrystals, Int. J. Fatigue. 68 (2014) 90–102. https://doi.org/10.1016/j.ijfatigue.2014.06.001.

[49] V.V.C. Wan, J. Jiang, D.W. MacLachlan, F.P.E. Dunne, Microstructure-sensitive fatigue crack nucleation in a polycrystalline Ni superalloy, Int. J. Fatigue. 90 (2016) 181–190. https://doi.org/10.1016/j.ijfatigue.2016.04.013.

[50] B. Chen, K. Janssens, F. Dunne, Multiaxial and non-proportional microstructure-sensitive fatigue crack nucleation, 12th Int. Conf. Multiaxial Fatigue Fract. (2019) 010001. https://doi.org/https://doi.org/10.1051/matecconf/201930001001.

[51] A. Heinz, P. Neumann, Crack initiation during high cycle fatigue of an austenitic steel, Acta Metall. Mater. 38 (1990) 1933–1940. https://doi.org/10.1016/0956-7151(90)90305-Z.

[52] J.C. Stinville, E. Martin, M. Karadge, S. Ismonov, M. Soare, T. Hanlon, S. Sundaram, M.P. Echlin, P.G. Callahan, W.C. Lenthe, V.M. Miller, J. Miao, A.E. Wessman, R. Finlay, A. Loghin, J. Marte, T.M. Pollock, Fatigue deformation in a polycrystalline nickel base superalloy at intermediate and high temperature: Competing failure modes, Acta Mater. 152 (2018) 16–33. https://doi.org/10.1016/j.actamat.2018.03.035.

[53] J. Miao, T.M. Pollock, J. Wayne Jones, Crystallographic fatigue crack initiation in nickel-based superalloy René 88DT at elevated temperature, Acta Mater. 57 (2009) 5964–5974. https://doi.org/10.1016/j.actamat.2009.08.022.